JOURNAL OF GUIDANCE, CONTROL, AND DYNAMICS
Vol. 32, No. 4, July–August 2009

Optimal Ascent Trajectories for Stratospheric Airships Using Wind Energy

Joseph B. Mueller,* Yiyuan J. Zhao,† and William L. Garrard‡
University of Minnesota, Minneapolis, Minnesota 55455

DOI: 10.2514/1.41270

Stratospheric airships are lighter-than-air vehicles that have the potential to provide an extremely-long-duration airborne presence at altitudes of 18–22 km. In this paper, we examine optimal ascent trajectories that use wind energy to achieve minimum-time and minimum-energy flights. The airship is represented by a three-dimensional point-mass model, and the equations of motion include aerodynamic lift and drag, vectored thrust, added mass effects, and accelerations due to mass-flow rate, wind rates, and Earth rotation. A representative wind profile is developed based on historical meteorological data and measurements. Trajectory optimization is performed by first defining an optimal control problem with both terminal and path constraints, then using direct collocation to develop an approximate nonlinear parameter optimization problem of finite dimension. Optimal ascent trajectories are determined using SNOPT for a variety of upwind, downwind, and crosswind launch locations. Results of extensive optimization solutions illustrate definitive patterns in the ascent path for minimum-time flights across varying launch locations and show that significant energy savings can be realized with minimum-energy flights, compared with minimum-time flights, given small increases in flight time. In addition, the effects of time-varying mass and Earth rotation are found to be comparable with the effects of wind rate, and they are used in the optimal solutions.

Nomenclature

B	=	buoyancy
C	=	rotation matrix from *ENU* to the wind frame
C_D	=	drag coefficient
C_L	=	lift coefficient
D	=	aerodynamic drag force
d_c	=	characteristic length for dimensional scaling
$\boldsymbol{E}$	=	translational velocity of the local *ENU* frame
ENU	=	east-north-up coordinate system
g	=	gravitational acceleration
h	=	altitude
k	=	scaling parameter
k_1	=	coefficient of added mass in longitudinal direction
k_2	=	coefficient of added mass in vertical/lateral directions
L	=	aerodynamic lift force
ℓ	=	longitude
m_a	=	variable mass of air inside the airship ballonets
m_{ax}	=	added mass components in the body-frame x direction
m_0	=	fixed mass of airship structure and helium
P	=	power
q	=	dynamic pressure
R	=	Earth radius
T	=	thrust
t_c	=	characteristic time for dimensional scaling
U_H	=	hull volume
$\boldsymbol{u}$	=	control vector
V	=	airship wind-relative velocity magnitude
$\boldsymbol{V}$	=	airship wind-relative velocity vector
V_c	=	characteristic velocity for dimensional scaling
$\boldsymbol{V}_X$	=	airship velocity with respect to frame X
W	=	weight
$\boldsymbol{W}$	=	wind velocity in the local *ENU* frame
W_E	=	wind speed in the east direction
W_N	=	wind speed in the north direction
$\boldsymbol{X}$	=	vector of decision variables
$\boldsymbol{x}$	=	state vector
α	=	angle of attack
γ	=	flight-path angle
η	=	combined efficiency of the propeller and motor
λ	=	latitude
μ	=	thrust vector pitch angle
ρ	=	atmospheric density
ϕ	=	bank angle
$\boldsymbol{\chi}$	=	path constraints
$\boldsymbol{\Psi}$	=	terminal constraints
ψ	=	heading
ω_E	=	Earth rotational rate
$\boldsymbol{\omega}_{L/I}$	=	rotational velocity of the Earth-fixed *ENU* frame with respect to inertial frame
$\boldsymbol{\omega}_{W/L}$	=	rotational velocity of the wind-relative frame with respect to the local *ENU* frame

Subscripts

c	=	characteristic unit
I	=	inertial frame
L	=	local frame

Received 26 September 2008; revision received 9 December 2008; accepted for publication 23 December 2008.

*Research Assistant; mueller@aem.umn.edu. Member AIAA.
†Professor, Aerospace Engineering and Mechanics; gyyz@aem.umn.edu. Associate Fellow AIAA.
‡Professor, Aerospace Engineering and Mechanics; wgarrard@aem.umn.edu. Fellow AIAA.

I. Introduction

STRATOSPHERIC airships are buoyant vehicles that can perform long-endurance station-keeping missions at the altitude range of 18–22 km in the calm portion of the lower stratosphere and above all regulated air traffic and cloud cover. This represents a unique operational platform that resides between conventional aircraft and low-Earth-orbiting (LEO) satellites. With the capability to maintain a fixed station at much lower altitudes than LEO or geostationary (GEO) satellites, the airship can provide enhanced performance for surveillance, communication, and remote-sensing missions that are traditionally assigned to spacecraft.

Because they operate in the low-density region of the stratosphere, airships must displace a large volume of air to achieve neutral buoyancy. The resulting design requires a large helium-filled hull,

which can nonetheless be used for harnessing solar energy by the integration of thin-film solar cells along the top and sides [1,2]. Recent advances in lightweight materials and energy-storage technologies have sparked serious interest in the stratospheric airship concept [3]. Several institutions have developed low- and midaltitude prototypes or test beds [4,5]. In recent years, numerous studies have been performed on airship design and feasibility [1,2,6–9], and a variety of methods have been proposed for trajectory tracking and feedback control design [10–14]. This widespread interest is reflective of the potential benefits in performance and cost that airships can offer over alternative systems.

On the other hand, a particular challenge for airship operation is the planning of ascent trajectories. Indeed, the slow-moving vehicle must traverse the high-wind region of the jet stream. Because of the large changes in wind across altitude and the susceptibility of airship motion to the wind, the trajectory must be carefully planned, preferably optimized, to ensure that the desired station is reached within acceptable performance bounds of flight time, energy consumption, and lateral excursion. However, very few studies have been conducted in this area to date.

Reference [15] generates paths of minimum distance that follow a prescribed set of waypoints, subject to kinematic constraints, and [16] computes helices as candidate paths for ascent that maintain trim conditions. However, neither of these studies account for the wind. In [17], minimum-energy and minimum-time trajectories are computed using a wind model of stacked homogeneous layers. This approach ignores the dynamics of the vehicle, assuming that only vertical control is used to enable the airship to traverse between wind layers, with horizontal motion governed completely by the wind.

In [18], optimal control problems were formulated for selected scenarios using a 3-degree-of-freedom point-mass model [19], and numerical solutions were developed to find optimal trajectories in the presence of horizontal winds. Although representing the first work of this type, to our knowledge, this initial study was limited in scope to high-altitude station transitions and station-keeping. In a recent paper [5], optimal ascent trajectories were designed for the Korean stratospheric airship, with both minimum-time and minimum-energy solutions, and the enforcement of a convex horizontal excursion constraint to keep the flight path within national borders. It is one of the few comprehensive publications of a stratospheric airship model, incorporating wind-tunnel test data, computational fluid dynamics analysis, and prototype flight data. However, it also has some important restrictions; namely, it does not consider the possibility of open initial or final positions, and it defines a performance index for the minimum-energy case that does not reflect the true energy consumption of the vehicle.

In this paper, we conduct a systematic study of optimal ascent trajectories of stratospheric airships. We first consider the scenario of fixed initial and final positions and illustrate the range of solutions between minimum-time and minimum-energy flights. We then extend this formulation to study optimal trajectories over a range of initial conditions. This provides crucial insights into the effect of wind gradients and reveals a general strategy for selecting the launch location. In all cases, the optimal control problem is converted into a nonlinear parameter optimization problem and solved numerically using SNOPT, a sparse nonlinear optimization solver that uses the sequential quadratic programming (SQP) technique.

The remainder of this paper is organized as follows. First, unique features and important operational considerations for airships are discussed. Airship equations of motion that then developed based on a point-mass model that include the presence of horizontal winds, added mass effects, and mass variation across altitude. Next, models for atmospheric density and horizontal winds are presented as a function of altitude based on actual measurement data. Optimal control problems are then formulated for minimum-time and minimum-energy airship flights. A collocation approach is used to transform the original problem formulations into parameter optimization problems, and numerical solutions are obtained using SNOPT. Extensive optimization results are obtained for different flight scenarios: a fixed point-to-point minimum-time ascent trajectory and a series of minimum-energy cases with different fixed-final times. Finally, optimal ascent trajectories are examined over a range of different launch locations for a fixed target, providing a general ascent strategy for given launch/target locations and wind conditions.

II. Baseline Design

Using buoyancy as the primary (sometimes sole) source of lift, airships are essentially controllable balloons. The first airship flights date back to the middle and late 19th century. Today's airships boast lighter materials and more powerful engines, but the basic principle remains the same.

The hull of the airship is filled with a light gas, making the entire vehicle lighter than air. Although the density of the vehicle is less than that of the surrounding atmosphere, the vehicle rises. This continues until the pressure altitude is reached at which the two densities are equal. Modern airships use a pressure regulation system, filling internal bags called *ballonets* with air at low altitudes. This equivalently regulates the vehicle density to be close to that of the ambient air, enabling controlled flight anywhere between the ground and pressure altitude [20].

Historically, airship structural designs have fallen into three general categories, based on the type of hull: rigid, semirigid, and nonrigid [20]. In rigid designs, such as the German zeppelins, the hull is composed of a solid structure. Airships with nonrigid hulls are also referred to as *pressurized airships*, because the flexible hull requires a slightly higher (about 1%) internal pressure to maintain its shape. A semirigid airship has a pressurized hull along with some additional internal structure. To maintain the stratospheric altitude of 20–22 km with buoyancy, the airship must be designed with an overall vehicle density of 0.06–0.08 $\mathrm{kg/m^3}$. This requires the hull surface density to be extremely low, so that only pressurized, nonrigid designs remain viable. This is evidenced in recent work by Lee and Bang [5], Schmidt et al. [2], and Schmidt [9].

We therefore assume for this study that the airship is of a semirigid design with a pressurized hull and additional structure for housing the payload and onboard systems, which include avionics, propulsion, power generation, and energy storage. In these configurations, the pressure regulation system causes the vehicle density to closely match the ambient density, so that the net static lift is nearly zero. In other words, the buoyancy force closely matches the weight throughout the flight envelope.

The baseline design configuration is summarized in Table 1. The hull is modeled as an ellipsoid that is symmetric about the longitudinal axis. The dimensions and aerodynamic properties are chosen to closely match those by Lee and Bang [5] to enable a meaningful comparison of the optimal trajectories. This design configuration, in terms of geometric dimensions and operating constraints, is found to be consistent with the authors' experience in feasibility studies of high-altitude airships.

III. Airship Equations of Motion

A. Unique Airship Features

Although the airship does share many common attributes with traditional aircraft, several properties are fundamentally different and

Table 1 Baseline airship design parameters

Design parameter	Symbol	Value
Pressure altitude	h_p	24 km
Length	l	200 m
Diameter	d	50 m
Volume	U_H	261,800 $\mathrm{m^3}$
Surface area	S	25,300 $\mathrm{m^2}$
Drag coefficient	C_{Do}	0.04
Maximum airspeed	$V_{\max}$	30 m/s
Maximum flight-path angle	$\gamma_{\max}$	30 deg
Maximum thrust	$T_{\max}$	10 kN
Maximum propulsion power	$P_{\max}$	100 kW
Maximum climb rate	$\dot{h}_{\max}$	10 m/s
Added mass coefficient, x axis	k_1	0.082
Added mass coefficient, y and z axes	k_2	0.860

must be understood to develop meaningful models and problem formulations.

By definition, the buoyancy force is equivalent to the weight of displaced air, and so

$$B = U_H \rho(h) g$$

The weight of the airship is

$$W = [m_0 + m_a(h)]g$$

To achieve static buoyancy, or zero net lift, the air mass inside the airship must change with altitude according to

$$m_a(h) = U_H \rho_a(h) - m_0 \tag{1}$$

The ceiling altitude, or pressure altitude, occurs when the ballonets fully deflate, where $m_a(h) = 0$, or

$$\rho_a(h) = m_0 / U_H$$

The rate at which air enters or leaves the ballonets is constrained by the capabilities of the fans in the pressure regulation system. This translates into imposed limits on the rate of ascent or descent, to maintain neutral buoyancy. In this paper, we assume that neutral buoyancy is maintained throughout the flight, which is equivalent to the assumption that the rate of airflow during ascent can be achieved by the pressure regulation system.

In addition, the required thrust and power change with flight condition, according to

$$T_{\text{req}} = D = \tfrac{1}{2}\rho(h) V^2 U_H^{2/3} C_{Do} \tag{2}$$

$$P_{\text{req}} = \frac{T_{\text{req}} V}{\eta} \tag{3}$$

where $U_H^{2/3}$ is the standard aerodynamic reference area for airships.

B. Kinematic Equations

The position of the airship is described in the topocentric local coordinate system ENU with unit vectors $[\boldsymbol{e}, \boldsymbol{n}, \boldsymbol{u}]$, pointing east, north, and up, respectively. Figure 1 illustrates the topocentric coordinates along with the Earth-centered inertial coordinates IJK with unit vectors $[\boldsymbol{I}, \boldsymbol{J}, \boldsymbol{K}]$. Note that ℓ is the Earth-relative longitude, and the Earth rotates around the $\boldsymbol{K}$ vector at the rate of ω_E.

Derivation of airship equations involves three velocity concepts: inertial velocity, Earth-relative or local velocity, and wind-relative velocity. Considering the rotation of the Earth, the inertial velocity is found by

$$\boldsymbol{V}_I = \boldsymbol{V}_L + \boldsymbol{E} \tag{4}$$

where $\boldsymbol{E} = \omega_E (R + h) \cos\lambda \boldsymbol{e}$. If the Earth rotation is assumed to be zero, then $\boldsymbol{E} = 0$ and $\boldsymbol{V}_I = \boldsymbol{V}_L$, meaning that the local frame becomes the inertial frame. We include the Earth rotation terms throughout this derivation to examine the size of the resulting acceleration terms. In addition, although the spherical-Earth effects are small considering the ranges involved in this study, including them in the equations of motion leads to a general-purpose model suitable for ascent and station-transfer planning over extremely large distances.

To obtain the inertial velocity, we differentiate the position vector with respect to the inertial IJK frame and express the result in the ENU frame. The position of the airship is

$$\boldsymbol{r} = (R + h)\boldsymbol{u} \tag{5}$$

The inertial velocity $\boldsymbol{V_I}$ is then given as

$$\boldsymbol{V}_I = \dot{\boldsymbol{r}} = \dot{h}\boldsymbol{u} + \boldsymbol{\Omega} \times \boldsymbol{r} = (\dot{\ell} + \omega_E)\cos\lambda (R + h)\boldsymbol{e} + \dot{\lambda}(R + h)\boldsymbol{n} + \dot{h}\boldsymbol{u} \tag{6}$$

where the angular velocity $\boldsymbol{\Omega}$ with respect to the inertial IJK frame is given by

$$\boldsymbol{\Omega} = (\dot{\ell} + \omega_E)\boldsymbol{K} - \dot{\lambda}\boldsymbol{e} = -\dot{\lambda}\boldsymbol{e} + (\dot{\ell} + \omega_E)\cos\lambda \boldsymbol{n} + (\dot{\ell} + \omega_E)\sin\lambda \boldsymbol{u} \tag{7}$$

An important consideration in this paper is the effect of steady-state horizontal winds. The horizontal-wind velocity vector is defined as

$$\boldsymbol{W} = W \sin\psi_W \boldsymbol{e} + W \cos\psi_W \boldsymbol{n} = W_E \boldsymbol{e} + W_N \boldsymbol{n} \tag{8}$$

Figure 2 illustrates the relationship between the horizontal-wind vector, the airspeed velocity vector, and the local (Earth-fixed) velocity of the airship. The wind-relative velocity vector is defined by the airspeed V, the flight-path angle γ, and the heading ψ. We distinguish the local and inertial velocity components with the L and I subscripts, respectively.

From Fig. 2, the velocity with respect to the local ENU frame is determined as

$$\boldsymbol{V}_L = \boldsymbol{V} + \boldsymbol{W} \tag{9}$$

$$\boldsymbol{V}_L = V\sin\gamma \boldsymbol{u} + (V\cos\gamma\sin\psi + W_E)\boldsymbol{e} + (V\cos\gamma\cos\psi + W_N)\boldsymbol{n} \tag{10}$$

$$\boldsymbol{V}_L = V_L \sin\gamma_L \boldsymbol{u} + V_L \cos\gamma_L \sin\psi_L \boldsymbol{e} + V_L \cos\gamma_L \cos\psi_L \boldsymbol{n} \tag{11}$$

Equating Eqs. (4) and (6) and using Eq. (10), we obtain the following kinematic relationships:

$$\dot{\ell}\cos\lambda(R + h) = V\cos\gamma\sin\psi + W_E = V_L \cos\lambda_L \sin\psi_L \tag{12}$$

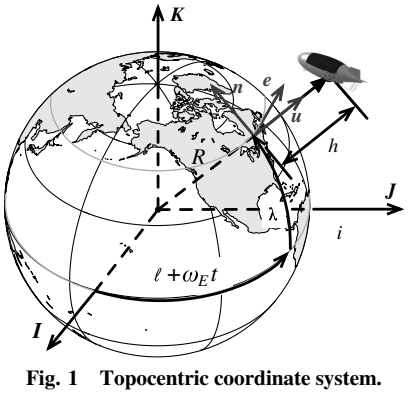

Fig. 1 Topocentric coordinate system.

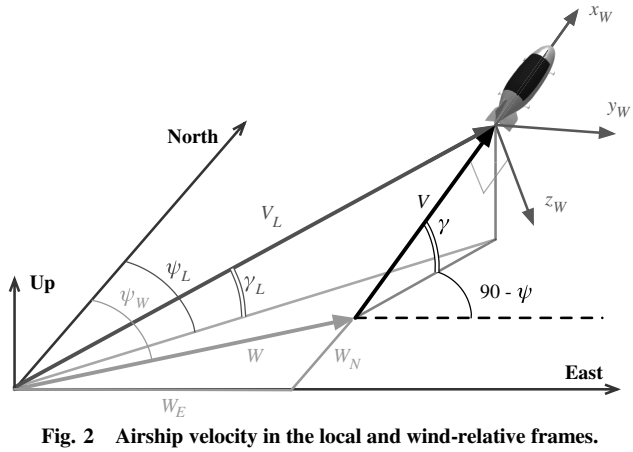

Fig. 2 Airship velocity in the local and wind-relative frames.

$$\dot{\lambda}(R+h) = V\cos\gamma\cos\psi + W_N = V_L\cos\lambda_L\cos\psi_L \tag{13}$$

$$\dot{h} = V\sin\gamma = V_L\sin\lambda_L \tag{14}$$

As shown in Fig. 2, the wind frame (xyz) is attached to the body of the airship and is rotated from the ENU frame through the flight-path angle γ and heading angle ψ. Note that the bank angle ϕ is assumed to be zero; the justification for this assumption is provided later in this section. The rotation matrix is therefore

$$\begin{bmatrix}\mathbf{x}\\ \mathbf{y}\\ \mathbf{z}\end{bmatrix} = \begin{bmatrix}\cos\gamma\sin\psi & \cos\gamma\cos\psi & \sin\gamma\\ \cos\psi & -\sin\psi & 0\\ \sin\gamma\sin\psi & \sin\gamma\cos\psi & -\cos\gamma\end{bmatrix}\begin{bmatrix}\mathbf{e}\\ \mathbf{n}\\ \mathbf{u}\end{bmatrix} = C\begin{bmatrix}\mathbf{e}\\ \mathbf{n}\\ \mathbf{u}\end{bmatrix} \tag{15}$$

C. External Forces

The external forces acting on the airship include aerodynamic lift L, drag D, thrust T, weight W, and buoyancy B. We also consider a generic lateral force N, which may be generated by any means, such as rolling the lift vector through a small angle ϕ or applying lateral thrust, for example. A free-body diagram of the forces in the x–z plane is shown in Fig. 3.

Note that the total mass of the airship changes significantly during ascent as the internal ballonets contract. A small additional thrust $\dot{m}V$ can be produced by ejecting air from the ballonets. The mass-flow rate $\dot{m}$ is found by differentiating Eq. (1) with respect to time:

$$\dot{m} = U_H\dot{\rho}(h) = U_H\frac{\partial\rho}{\partial h}\dot{h} \tag{16}$$

Although the resulting force created by this mass flow will be small compared with the propeller thrust, it is included in this model to examine the potential for exploiting this momentum transfer in trajectory planning. The practical considerations of implementation and net benefits should be evaluated more fully in the context of a vehicle design study.

The sum of forces in the wind-relative frame is

$$\Sigma\boldsymbol{F} = [(B-W)\sin\gamma + T\cos(\alpha+\mu) - D]\hat{x} + N\hat{y} + [(W-B)\cos\gamma - L - T\sin(\alpha+\mu)]\hat{z} \tag{17}$$

where the lift and drag forces are defined as $L = qU_H^{2/3}C_L(\alpha)$ and $D = qU_H^{2/3}C_D(\alpha)$, respectively. The lift and drag coefficients from Lee and Bang [5] are used and are assumed to vary only with angle of attack.

D. Dynamics

The equations of motion are described by equating the time derivative of the momentum vector with the sum of external forces:

$$\Sigma\boldsymbol{F} = \frac{d}{dt}(M\boldsymbol{V}_I) \tag{18}$$

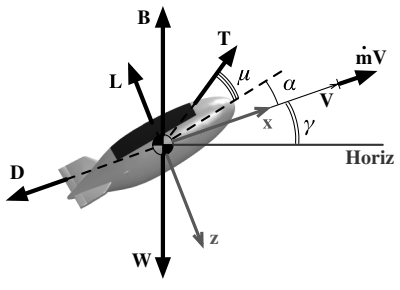

Fig. 3 External forces acting on the airship.

For an airship, we must use a mass tensor M to account for the different effects of added mass in each axis. This phenomena is based on the fact that any object accelerating through a fluid must also accelerate some of the surrounding fluid. For traditional aircraft, the mass of the surrounding fluid is negligible compared with the mass of the vehicle. For airships, however, the added mass effect is significant and must be included. The mass tensor is defined as

$$M = m[I] + \begin{bmatrix}k_1 & 0 & 0\\ 0 & k_2 & 0\\ 0 & 0 & k_3\end{bmatrix}\rho(h)U_H = \begin{bmatrix}m+m_{ax} & 0 & 0\\ 0 & m+m_{ay} & 0\\ 0 & 0 & m+m_{az}\end{bmatrix} \tag{19}$$

where k_1, k_2, and k_3 are added mass coefficients that can be derived from the geometry of the vehicle [21], and m is the scalar total mass of the airship structure and internal gas. For an airship that is symmetric about the x axis, $k_2 = k_3$.

The total inertial acceleration is the acceleration of the airship with respect to the local ENU frame, plus the acceleration of the ENU frame in inertial space, plus the Coriolis acceleration. Using the notation $(d\cdot/dt)_A$ to denote a derivative taken with respect to frame A, the inertial acceleration expressed in the wind frame is

$$\left(\frac{d\boldsymbol{V}_I}{dt}\right)_I = \left(\frac{d\boldsymbol{V}_L}{dt}\right)_L + \boldsymbol{\omega}_{L/I}\times\boldsymbol{V}_L + \left(\frac{d\boldsymbol{E}}{dt}\right)_I \tag{20}$$

Now define $\boldsymbol{V} = [V,0,0]^T$ to be the expression of the wind-relative velocity vector in the wind frame. Also, let $\boldsymbol{\omega}_{W/L}$ be the angular rotation of the wind frame with respect to ENU, and let $\boldsymbol{\omega}_{L/I}$ be the angular velocity of ENU with respect to the inertial frame. The first two terms of Eq. (20) are then expanded as follows:

$$\left(\frac{d\boldsymbol{V}_L}{dt}\right)_L = \left(\frac{d\boldsymbol{V}}{dt}\right)_W + \boldsymbol{\omega}_{W/L}\times\boldsymbol{V} + \left(\frac{d\boldsymbol{W}}{dt}\right)_L \tag{21}$$

$$\left(\frac{d\boldsymbol{E}}{dt}\right)_I = \left(\frac{d\boldsymbol{E}}{dt}\right)_L + \boldsymbol{\omega}_{L/I}\times\boldsymbol{E} \tag{22}$$

where the angular velocities and the wind velocity derivative are defined as

$$\boldsymbol{\omega}_{L/I} = \omega_E(\cos\lambda\boldsymbol{n} + \sin\lambda\boldsymbol{u}) \tag{23}$$

$$\boldsymbol{\omega}_{W/L} = -\dot{\psi}\sin\gamma\boldsymbol{e} + \dot{\gamma}\boldsymbol{n} + \dot{\psi}\cos\gamma\boldsymbol{u} \tag{24}$$

$$\left(\frac{d\boldsymbol{W}}{dt}\right)_L = \dot{\boldsymbol{W}} = \dot{W}_E\boldsymbol{e} + \dot{W}_N\boldsymbol{n} \tag{25}$$

$$\left(\frac{d\boldsymbol{E}}{dt}\right)_L = \dot{\boldsymbol{E}} = \omega_E(\dot{h}\cos\lambda - (R+h)\sin\lambda\dot{\lambda})\boldsymbol{e} \tag{26}$$

The wind rate terms are simply the product of the wind gradient across altitude and the altitude rate [e.g., $\dot{W}_E = (\partial W_E/\partial h)\dot{h}$]. The resulting expression for the inertial acceleration is

$$\left(\frac{d\boldsymbol{V}_I}{dt}\right)_I = \left(\frac{d\boldsymbol{V}}{dt}\right)_W + \boldsymbol{\omega}_{W/L}\times\boldsymbol{V} + \boldsymbol{\omega}_{L/I}\times\boldsymbol{V}_L + \left(\frac{d\boldsymbol{W}}{dt}\right)_L + \left(\frac{d\boldsymbol{E}}{dt}\right)_L + \boldsymbol{\omega}_{L/I}\times\boldsymbol{E} \tag{27}$$

E. Complete Equations of Motion

The complete equations of motion of the airship include the rate of change of its geographic position, provided in the kinematic equations (12–14), and the rate of change of its wind-relative velocity. The velocity vector derivative is found by differentiating Eq. (4) with respect to the inertial frame and expressing the result in the wind frame.

Expanding Eq. (27) with Eqs. (17) and (18), we obtain the following expressions for the time-rate of change of the wind-relative velocity components:

$$\dot{V} = \frac{(B - W)\sin\gamma + T\cos\alpha - D - U_H\rho\dot{V}}{m + m_{ax}} - \dot{W}_x - a_{Ex} \tag{28}$$

$$\dot{\gamma} = \frac{(B - W)\cos\gamma + T\sin\alpha + L}{(m + m_{az})V} + \frac{\dot{W}_z + a_{Ez}}{V} \tag{29}$$

$$\dot{\psi} = \frac{N}{(m + m_{ay})V\cos\gamma} - \frac{\dot{W}_y + a_{Ey}}{V\cos\gamma} \tag{30}$$

where the wind rate terms in the wind frame are

$$\dot{W}_x = \dot{W}_E\cos\gamma\sin\psi + \dot{W}_N\cos\gamma\cos\psi \tag{31}$$

$$\dot{W}_y = \dot{W}_E\cos\gamma - \dot{W}_N\sin\gamma \tag{32}$$

$$\dot{W}_z = \dot{W}_E\sin\gamma\sin\psi + \dot{W}_N\sin\gamma\cos\psi \tag{33}$$

The additional acceleration due to the rotation of the Earth is

$$\boldsymbol{a}_E = \begin{bmatrix} a_{Ex} \\ a_{Ey} \\ a_{Ez} \end{bmatrix} = \boldsymbol{\omega}_{L/I} \times \boldsymbol{V}_L + \left(\frac{d\boldsymbol{E}}{dt}\right)_L + \boldsymbol{\omega}_{L/I} \times \boldsymbol{E} \tag{34}$$

The expanded form of the acceleration terms due to rotation of the Earth are

$$\begin{aligned} a_{Ex} = {} & \omega_E\{(W_E + V)(\sin\lambda\cos\gamma\cos\psi - \cos\lambda\sin\gamma) \\ & - 2W_N\sin\lambda\cos\gamma\sin\psi\} + \omega_E^2(R + h)\cos\lambda \\ & \times (\cos\gamma\cos\psi\sin\lambda - \sin\gamma\cos\lambda) \end{aligned} \tag{35}$$

$$\begin{aligned} a_{Ey} = {} & \omega_E\{-W_E\sin\lambda\sin\psi - 2W_N\sin\lambda\cos\psi \\ & + V(\cos\lambda\sin\gamma\cos\psi - \sin\gamma\cos\psi(1 - \cos^2\psi))\} \\ & - \omega_E^2(R + h)\cos\lambda\sin\psi\sin\lambda \end{aligned} \tag{36}$$

$$\begin{aligned} a_{Ez} = {} & \omega_E\{W_E(\sin\lambda\sin\gamma\cos\psi + \cos\lambda\cos\gamma) \\ & - 2W_N\sin\lambda\sin\gamma\sin\psi\} + \omega_E\{V(\cos\lambda\sin\psi(1 + \sin^2\gamma) \\ & - \sin\lambda\sin\gamma\cos\gamma\sin\psi\cos\psi)\} + \omega_E^2(R + h) \\ & \times \cos\lambda(\sin\gamma\cos\psi\sin\lambda + \cos\gamma\cos\lambda) \end{aligned} \tag{37}$$

F. Dimensional Scaling

To effectively use any numerical optimization routine, it is important to first scale the variables of the problem. Simply put, the objective is to scale all of the variables so that they are neither very small nor very large. In this problem, a common set of dimensional scalings is applied for time, length, velocity, and acceleration. The characteristic scales are defined as

$$d_c = \frac{R}{k^2}, \qquad V_c = \frac{\sqrt{gR}}{k}, \qquad t_c = \frac{1}{k}\sqrt{\frac{R}{g}} \tag{38}$$

where $k > 0$ is a scaling constant, chosen to provide a balanced scaling of variables throughout the dynamics and constraint equations. Note that the scales are consistent, such that $V_c = d_c/t_c$ and $g = V_c/t_c$. The normalized variables are defined as

$$\bar{V} = \frac{V}{V_c}, \qquad \bar{h} = \frac{h}{d_c}, \qquad \tau = \frac{t}{t_c} \tag{39}$$

$$\bar{W}_E = \frac{W_E}{V_c}, \qquad \bar{W}_N = \frac{W_N}{V_c} \tag{40}$$

$$\bar{T} = \frac{T}{U_H\rho(h_0)g}, \qquad \bar{\rho}(\bar{h}) = \frac{\rho(h)}{\rho(h_0)} \tag{41}$$

and the normalized lift and drag forces are expressed as

$$\bar{L} = \frac{L}{U_H\rho(h)g} = AC_L(\alpha)\bar{V}^2 \tag{42}$$

$$\bar{D} = \frac{D}{U_H\rho(h)g} = AC_D(\alpha)\bar{V}^2 \tag{43}$$

where $A = d_c/\left(2U_H^{1/3}\right)$. Additionally, the normalized time derivative is related to the original time derivative as follows:

$$()' = \frac{d()}{d\tau} = t_c\frac{d()}{dt} = t_c\dot{()} \Rightarrow ()' = \frac{1}{k}\sqrt{\frac{R}{g}}\dot{()}$$

After some algebra, the complete set of equations can now be written in nondimensional form as follows:

$$\begin{aligned} \bar{V}' = {} & \frac{1}{1 + k_1}\left\{\frac{\bar{T}\cos(\alpha + \mu) - (\partial\bar{\rho}/\partial\bar{h})\sin\gamma\bar{V}^2}{\bar{\rho}(\bar{h})} - AC_D(\alpha)\bar{V}^2\right\} \\ & - \frac{\partial\bar{W}_x}{\partial\bar{h}}\bar{V}\sin\gamma - \bar{a}_{Ex} \end{aligned} \tag{44}$$

$$\gamma' = \frac{1}{1 + k_2}\left\{\frac{\bar{T}\sin(\alpha + \mu)}{\bar{\rho}(\bar{h})\bar{V}} + AC_L(\alpha)\bar{V}\right\} + \frac{\partial\bar{W}_z}{\partial\bar{h}}\sin\gamma + \bar{a}_{Ez}/\bar{V} \tag{45}$$

$$\ell' = \frac{\bar{V}\cos\gamma\sin\psi + \bar{W}_E}{\cos\lambda(\bar{R} + \bar{h})} \tag{46}$$

$$\lambda' = \frac{\bar{V}\cos\gamma\cos\psi + \bar{W}_N}{(\bar{R} + \bar{h})} \tag{47}$$

$$\bar{h}' = \bar{V}\sin\gamma \tag{48}$$

G. Assumptions

We first discuss the omission of bank angle in these equations. Traditional aircraft turn by banking, which rotates the lift vector to

create lateral acceleration. However, this form of turning is not necessarily the best option for airships, for at least three reasons. First, airships produce much less dynamic lift than traditional aircraft, as airships rely primarily on buoyancy for the lifting force. Second, the combination of the weight and buoyancy forces creates a natural stabilizing moment about the roll axis, as the center of buoyancy is located above the center of gravity. This stabilizing moment must be overcome to hold a nonzero bank angle over time. To perform this maneuver aerodynamically would require large control surfaces, which, for the stratospheric airship, would bring a significant increase weight and drag. Third, the types of payloads for station-keeping missions will likely be Earth-pointing or zenith-pointing. Large bank angles would tend to violate these payload pointing requirements for fixed mounted payloads, whereas pure yaw maneuvers would pose no problem. It is therefore reasonable to consider other mechanisms for turning that do not rely on bank angle, such as differential thrust to turn with sideslip or pure lateral thrust. The inherent roll limitation is evidenced in [5], in which bank angle is used as a control input, but with a limit of only 5 deg. As a consequence of these practical airship design constraints, we assume that the bank angle remains sufficiently close to zero such that it can be ignored in the equations of motion.

In this paper, we assume that the airship regulates internal pressure to maintain zero static lift ($B = W$) throughout the flight envelope. The longitudinal control inputs are angle of attack α, thrust T, and thrust vector angle μ. We choose the lateral control input to be heading ψ, and we enforce bounds on $\dot{\psi}$. The states of the system are the wind-relative velocity V, flight-path angle γ, and geographic position $[\ell, \lambda, h]$. Therefore, the state equations for the system include the kinematic expressions (12–14) and the longitudinal velocity derivatives (28) and (29).

To summarize, this formulation of the airship equations of motion includes the point-mass kinematic equations for a spherical Earth, steady-state horizontal winds that vary with altitude, longitudinal dynamics governed by lift, drag and vectored thrust, mass variation with altitude, the effects of added mass, and virtual accelerations due to the wind variations and Earth rotation. This formulation is more general than the model provided by Lee and Bang [5], in that it includes Earth rotation and mass variation across altitude. Also note that the dynamic relationship of $\dot{\psi}$ with the other states and controls, given in Eq. (30), can be used as a time-varying constraint if desired. However, for this study, we impose constant bounds on $\dot{\psi}$.

IV. Environmental Models

The stratospheric airship must fly through a wide range of flight conditions, from 0 to 30 m/s airspeed, and from sea level to about a 21 km altitude. During its ascent, the atmospheric density drops by a factor of 16 from 1.225 to about 0.075 kg/m^3. In this paper, we assume that the atmospheric density changes with altitude according to the standard atmosphere model [22]. A third-order polynomial is fit to the standard atmosphere data over an altitude range of 0 to 23 km. The altitude is normalized before fitting to obtain better numerical accuracy. The polynomial expression is given as

$$\rho(h) = \rho(0)[c_0 + c_1(h/d_c) + c_2(h/d_c)^2 + c_3(h/d_c)^3] \tag{49}$$

where d_c is a dimensional scaling parameter, defined in Eq. (38). Using $d_c = 15,891.915$ km and

$$\boldsymbol{c} = [-0.11159, 0.71537, -1.45854, 0.99523]^T$$

gives a maximum error of 2.6% and a mean error of 0.84%.

The winds also change considerably with altitude. The general trend is that windspeed gradually increases as we ascend through the troposphere, reaching a peak in the jet-stream altitude range of 10–15 km. It then gradually decreases again to reach a minimum speed in the lower portion of the stratosphere, generally between 18–25 km. The actual wind profile changes with geographic location and the time of year and is also effected by the 11-year solar cycle.

In general, wind velocity can be split into steady-state and time-varying components. Although the actual winds encountered during flight cannot be predicted exactly, steady-state horizontal winds are known to follow specific trends with altitude, geographic position, and the time of year. Typical wind behavior can be adequately characterized based upon meteorological data, which provides a mechanism for design-phase planning. In addition, weather balloons and other instruments can be used immediately before flight for preflight and onboard planning.

The 1993 horizontal-wind model (HWM93), produced by the U.S. Naval Research Laboratory (NRL), uses a combination of historical meteorological data and measurements from radar and rocket sounding experiments to develop an analytic empirical model [23]. A FORTRAN program of the HWM93[§] was used to generate wind profiles over altitude at select times and geographic locations. In this paper, we use the HWM93 to model the average wind profile at the coordinates of 118°0.0′ W, 35°0.0′ N. This is located at the southern end of Edwards Air Force Base, approximately 100 km north of Los Angeles. The variation of the east component of wind across altitude is shown in Fig. 4 for four different times of year. The north component of the wind is not shown, as the maximum speed is under 1 m/s. This is representative of the typical wind profile observed in the continental United States, with the peak speeds occurring in the jet-stream altitude range of 10–15 km and with the wind directed primarily eastward.

The east and north components of the wind are fit to the HWM93 data using seventh-order polynomials. As before, the polynomial is fit after normalizing the altitude and velocity with constant scaling parameters. The expression for the east wind approximation is

$$W_E(h) = V_c\Big[c_{e0} + c_{e1}(h/d_c) + c_{e2}(h/d_c)^2 + \cdots + c_{e7}(h/d_c)^7\Big] \tag{50}$$

The north wind is found with the same polynomial expression, but with the $\boldsymbol{c}_n$ coefficients. Using $d_c = 15,891.915$ km and $V_c =$ 395.04 m/s, we obtain the following coefficients for the winter-season wind model:

$$\boldsymbol{c}_e = [-0.16235, 0.83550, -1.64017, 1.60473, -0.89284 \quad 0.20646, 0.09708, 0.00246]^T \tag{51}$$

$$\boldsymbol{c}_n = [-0.00103, 0.00502, -0.00789, 0.00459, -0.00104 \quad -0.00085, 0.00047, -0.00001]^T \tag{52}$$

The approximations match the original model, with a maximum error of 0.4% in the east component and 1.1% in the north component.

V. Formulations for Optimal Airship Flights

We now consider the formulation of trajectory optimization problems for various types of airship flights. Let the state vector $\boldsymbol{x}(t)$ and control vector $\boldsymbol{u}(t)$ be defined as

$$\boldsymbol{x}(t) = [V, \gamma, \ell, \lambda, h]^T \tag{53}$$

$$\boldsymbol{u}(t) = [T, \alpha, \mu, \psi]^T \tag{54}$$

The airship dynamic model is described by the system of nonlinear differential equations given in Eqs. (12–14), (28), and (29), which can be expressed as

$$\dot{\boldsymbol{x}}(t) = f(\boldsymbol{x}(t), \boldsymbol{u}(t), t) \tag{55}$$

The optimization problem is to choose a control history $\boldsymbol{u}(t)$ that minimizes a scalar performance index J, subject to the equations of motion over some time interval $[t_0, t_f]$, and other constraints that may

[§]Data available at http://uap-www.nrl.navy.mil/uap/ [retrieved 20 January 2009].

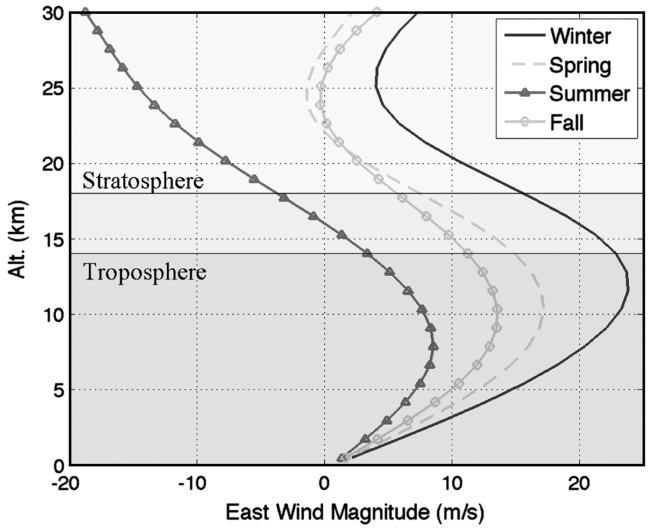

Fig. 4 HWM93 wind prole over southern California.

be enforced on the states and controls. Specifically, we enforce constant bounds on the states, controls, and control rates and impose both path constraints $\boldsymbol{\chi}$ and terminal constraints $\boldsymbol{\Psi}$ on the state. The problem is summarized as

$$\begin{aligned} &\min_{\boldsymbol{u}(t),t\in[t_0,t_f],t_f} \quad J(\boldsymbol{x}(t),\boldsymbol{u}(t),t) \\ &\text{subject to} \quad \dot{\boldsymbol{x}}(t)=f(\boldsymbol{x}(t),\boldsymbol{u}(t),t),\boldsymbol{x}(t_0)\in\boldsymbol{X}_0 \\ &\boldsymbol{x}_L\le\boldsymbol{x}(t)\le\boldsymbol{x}_U, t>t_0, \qquad \boldsymbol{u}_L\le\boldsymbol{u}(t)\le\boldsymbol{u}_U \\ &\dot{\boldsymbol{u}}_L\le\dot{\boldsymbol{u}}(t)\le\dot{\boldsymbol{u}}_U, \qquad \boldsymbol{\chi}(\boldsymbol{x}(t))\le 0, \qquad \boldsymbol{\Psi}(\boldsymbol{x}(t_f))=0 \end{aligned} \tag{56}$$

where $\boldsymbol{X}_0$ represents an allowable set of initial states. The path constraints include bounds on the climb rate and power, as given next:

$$\boldsymbol{\chi}_1 = V\sin\gamma-\dot{h}_{\max}\le 0 \tag{57}$$

$$\boldsymbol{\chi}_2 = TV-P_{\max}\eta\le 0 \tag{58}$$

The terminal constraint enforces a final desired position (ℓ_f,λ_f,h_f) and speed (V_{Lf}) to be achieved:

$$\boldsymbol{\Psi}_1=\ell(t_f)-\ell_f=0 \tag{59}$$

$$\boldsymbol{\Psi}_2=\lambda(t_f)-\lambda_f=0 \tag{60}$$

$$\boldsymbol{\Psi}_3=h(t_f)-h_f=0 \tag{61}$$

$$\boldsymbol{\Psi}_4=(V\cos\gamma\cos\psi+W_N)^2+(V\cos\gamma\sin\psi+W_E)^2-V_{Lf}^2=0 \tag{62}$$

In the present paper, we focus on two different types of optimal ascent trajectories: minimum time and minimum energy. Within the context of feedback control design, the term *energy* is indeed often referred to as the total control effort, $\int u^2(t)\mathrm{d}t$. However, this is not necessarily meaningful for airship trajectory planning, as it does not reflect the true energy expenditure of the airship during flight. The total energy consumption of the airship during the trajectory is the integral of the required power:

$$E=\int_{t_0}^{t_f}\frac{VT}{\eta}\mathrm{d}t \tag{63}$$

Here, we consider only the power required for propulsion, ignoring any power required for payload and or systems operation, as these are expected to be small in comparison and are not affected by the trajectory. It is reasonable to assume that the efficiency remains constant throughout the flight, allowing it to be disregarded in the performance index. We can now define the performance index as

$$J=K_t t_f+K_p\int_{t_0}^{t_f}VT\mathrm{d}t \tag{64}$$

where K_t and K_p are nonnegative weighting coefficients that enable the problem to be cast as pure minimum time ($K_t=1$ and $K_p=0$), pure minimum energy ($K_t=0$ and $K_p=1$), or a blend of both objectives ($K_t>0$ and $K_p>0$).

Note that a more comprehensive model of the airship flight power requirement would include the power required to operate the pressure regulation system, which must blow air out of the ballonets during ascent. Providing a more accurate power model would help to design more realistic trajectories for the minimum-energy problem. In addition, it may be worthwhile to model the maximum airflow rate as a constraint. This would allow the buoyancy and weight to be modeled separately, with mass as a state, so that neutral-buoyancy conditions are only achieved when the pressure regulation system can expel or intake air fast enough.

VI. Numerical Solution Methods

The optimal control problem described previously can only be solved numerically. An effective method for developing a numerical solution is to transform this dynamic optimization problem into a parameter optimization problem. We use a collocation approach, discretizing the dynamic equations so that both the states and controls become decision variables over a finite number of nodes [24–26]. We then solve the problem numerically using SNOPT, which is a SQP tool that exploits the sparsity structure of the Jacobian matrix [27].

Define the time interval $t\in[t_0,t_f]$ over N nodes, so that $t_k=t_0+\bar{\tau}_k t_f$, where

$$0=\bar{\tau}_1<\bar{\tau}_2<\bar{\tau}_3<\cdots\bar{\tau}_{N-1}<\bar{\tau}_N=1$$

The state and control vectors at time t_k are now defined as $\boldsymbol{x}_k\in\mathbb{R}^{N_S}$ and $\boldsymbol{u}_k\in\mathbb{R}^{N_C}$, respectively. The vector of decision variables is composed of the states and controls over all nodes, as well as the final time t_f, so that $\boldsymbol{X}\in\mathbb{R}^{N_D}$ with $N_D=N(N_S+N_C)+1$:

$$\boldsymbol{X}=\left[\boldsymbol{x}_1^T,\boldsymbol{x}_1^T,\boldsymbol{u}_2^T,\boldsymbol{u}_2^T,\ldots,\boldsymbol{x}_N^T,\boldsymbol{u}_N^T,t_f\right] \tag{65}$$

We can now use Simpson's rule to integrate the dynamic equations. The original dynamic constraint is $\dot{\boldsymbol{x}}(t)=\boldsymbol{f}(\boldsymbol{x}(t),\boldsymbol{u}(t),t)$. Applying Simpson's rule to the discrete system, we have

$$\dot{\boldsymbol{x}}_k\approx\frac{\boldsymbol{x}_{k+1}-\boldsymbol{x}_k}{\Delta t_k}=\frac{1}{6}[\boldsymbol{f}_k+4\boldsymbol{f}_{mk}+\boldsymbol{f}_{k+1}] \tag{66}$$

where

$$\boldsymbol{f}_k=\boldsymbol{f}(\boldsymbol{x}_k,\boldsymbol{u}_k) \tag{67}$$

$$\boldsymbol{f}_{mk}=\boldsymbol{f}(\boldsymbol{x}_{mk},\boldsymbol{u}_{mk}) \tag{68}$$

Table 2 Solution parameters

Parameter	Value
k	20
R	6,356,766.0 m
g	9.82 m/s/s
V_c	395.0425 m/s
d_c	15,891.915 m
t_c	40.228 s

Table 3 Problem bounds

Minimum	Variable	Maximum	Units
0.1	V	30	m/s
−30	γ	30	deg
−10	$\dot{h}$	10	m/s
0	P	100	kW
0	T	10	kN
−10	α	10	deg
−90	μ	90	deg
−0.5	$\dot{\alpha}$	0.5	deg/s
−3.0	$\dot{\mu}$	3.0	deg/s
−1.0	$\dot{T}$	1.0	kN/s
−0.6	$\dot{\psi}$	0.6	deg/s

$$\boldsymbol{x}_{mk} = \tfrac{1}{2}(\boldsymbol{x}_k + \boldsymbol{x}_{k+1}) - \tfrac{1}{8}(\boldsymbol{f}_{k+1} - \boldsymbol{f}_k)\Delta t_k \tag{69}$$

$$\boldsymbol{u}_{mk} = \tfrac{1}{2}(\boldsymbol{u}_k + \boldsymbol{u}_{k+1}) \tag{70}$$

$$\Delta t_k = (\bar{\tau}_{k+1} - \bar{\tau}_k)t_f \tag{71}$$

These equations of motion provide a set of nonlinear constraint equations, $\boldsymbol{C}_f(\boldsymbol{X}) = 0$. Rearranging Eq. (66), the kth set of equations is given as

$$\boldsymbol{C}_{f,k} = \boldsymbol{x}_{k+1} - \boldsymbol{x}_k - \tfrac{1}{6}[\boldsymbol{f}_k + 4\boldsymbol{f}_{mk} + \boldsymbol{f}_{k+1}]\Delta t_k = 0 \qquad k \in [1, N-1] \tag{72}$$

The performance index, originally defined in Eq. (64), is now equivalently defined as

$$J(\boldsymbol{X}) = K_t t_f + K_p \sum_{k=1}^{N-1} T_k V_k \tag{73}$$

The parameter optimization problem is to choose a decision vector $\boldsymbol{X}$ that minimizes the preceding performance index, subject to a set of nonlinear constraints of the form $\boldsymbol{l} \le \boldsymbol{C}(\boldsymbol{X}) \le \boldsymbol{u}$, where $\boldsymbol{l}$ and $\boldsymbol{u}$ are fixed lower and upper bounds, respectively. The full set of constraints includes the equations of motion, the control rate limits, path constraints on climb rate and power, and the terminal constraints $\boldsymbol{C}_t$. The problem can now be stated as

$$\begin{aligned} \min_{\boldsymbol{X}} \quad & J(\boldsymbol{X}) \qquad \text{subject to} \quad \boldsymbol{f}_L \le \boldsymbol{C}_f(\boldsymbol{X}) \le \boldsymbol{f}_U \\ & \boldsymbol{c}_L \le \boldsymbol{C}_c(\boldsymbol{X}) \le \boldsymbol{c}_U, \qquad \boldsymbol{p}_L \le \boldsymbol{C}_p(\boldsymbol{X}) \le \boldsymbol{p}_U \\ & \boldsymbol{t}_L \le \boldsymbol{C}_t(\boldsymbol{X}) \le \boldsymbol{t}_U, \qquad \boldsymbol{X}_L \le \boldsymbol{X} \le \boldsymbol{X}_U \end{aligned} \tag{74}$$

where $\boldsymbol{X}_L$ and $\boldsymbol{X}_U$ are the lower and upper bounds on the decision variables across all nodes, $\boldsymbol{C}_c \in \mathbb{R}^{(N-1)N_C}$ is the set of rate limits on N_C controls, $\boldsymbol{C}_p \in \mathbb{R}^{NN_P}$ is the set of N_P path constraints over N nodes, and $\boldsymbol{C}_t \in \mathbb{R}^{N_T}$ is the set of N_T terminal constraints. Here, $N_P = 2$ for path constraints on climb rate and power, and $N_T = 4$ for terminal constraints on latitude, longitude, altitude, and inertial airspeed. The bounds on the initial state are included in $\boldsymbol{X}_L$ and $\boldsymbol{X}_U$.

The kth set of dynamic constraints is given in Eq. (72). Because these are equality constraints, we have $\boldsymbol{f}_L = \boldsymbol{f}_U = 0$. The kth set of control rate bounds, expressed as $\boldsymbol{c}_{L,k} \le \boldsymbol{C}_{c,k} \le \boldsymbol{c}_{U,k}$, is given as

$$\begin{bmatrix} \dot{T}_{\min} \\ \dot{\alpha}_{\min} \\ \dot{\mu}_{\min} \\ \dot{\psi}_{\min} \end{bmatrix} \le \begin{bmatrix} (T_{k+1} - T_k)/\Delta t_k \\ (\alpha_{k+1} - \alpha_k)/\Delta t_k \\ (\mu_{k+1} - \mu_k)/\Delta t_k \\ (\psi_{k+1} - \psi_k)/\Delta t_k \end{bmatrix} \le \begin{bmatrix} \dot{T}_{\max} \\ \dot{\alpha}_{\max} \\ \dot{\mu}_{\max} \\ \dot{\psi}_{\max} \end{bmatrix} \qquad k \in [1, N-1] \tag{75}$$

The kth set of path constraints is taken from Eqs. (57) and (58), so that $\boldsymbol{p}_{L,k} \le \boldsymbol{C}_{p,k} \le \boldsymbol{p}_{U,k}$ is equivalent to

$$\begin{bmatrix} \dot{h}_{\min} \\ 0 \end{bmatrix} \le \begin{bmatrix} V_k \sin\gamma_k \\ T_k V_k \end{bmatrix} \le \begin{bmatrix} \dot{h}_{\max} \\ P_{\max} \end{bmatrix}, \qquad k \in [1, N] \tag{76}$$

Finally, the terminal constraints are taken from Eqs. (59–62). As with the dynamics, these are enforced as equality constraints, and so $\boldsymbol{t}_L = \boldsymbol{t}_U = 0$.

For numerical solutions, we discretize the problem over 60 nodes and use SNOPT to compute optimal trajectories for various sets of initial conditions and cost functions.

VII. Numerical Results

For all problems considered, the target position is fixed at 35° latitude, −118° longitude, and 21.334 km altitude. We impose an additional terminal constraint that the final Earth-relative velocity be less than 10 m/s. The airship is initialized in level flight at 1 m/s airspeed and at an altitude of 710 m to match the local elevation. The initial heading is open. The scaling parameters and constants are defined in Table 2, and the bounds on state variables, control inputs, control rates, climb rate, and supplied power are provided in Table 3.

In solving the optimal control problems, we neglect the contribution from centripetal acceleration [those terms from Eqs. (36–38) with ω_E^2]. This acceleration is constant in the ENU frame, with a magnitude of 0.029 m/s^2, and components only in the north/south and vertical directions. The upward vertical component is assumed to be a tiny part of the buoyancy that cancels with gravity. The component in the north/south direction acts in the lateral direction of the airship for east/west flights, with a magnitude of about 0.014 m/s/s. These are the only flights considered in this paper for minimum-energy scenarios, in which the Earth acceleration terms can be significant. We ignore this lateral component in the optimization because it is easily dominated by lateral forces and it cannot be exploited for east/west flights.

Next, we consider four different types of ascent scenarios, all with the same target location but with different initial conditions and different flight objectives.

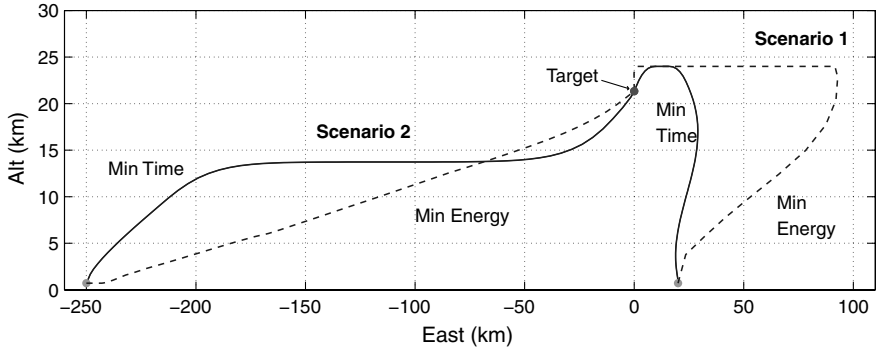

Fig. 5 Scenarios 1 and 2, minimum-time and fixed-time/minimum-energy trajectories.

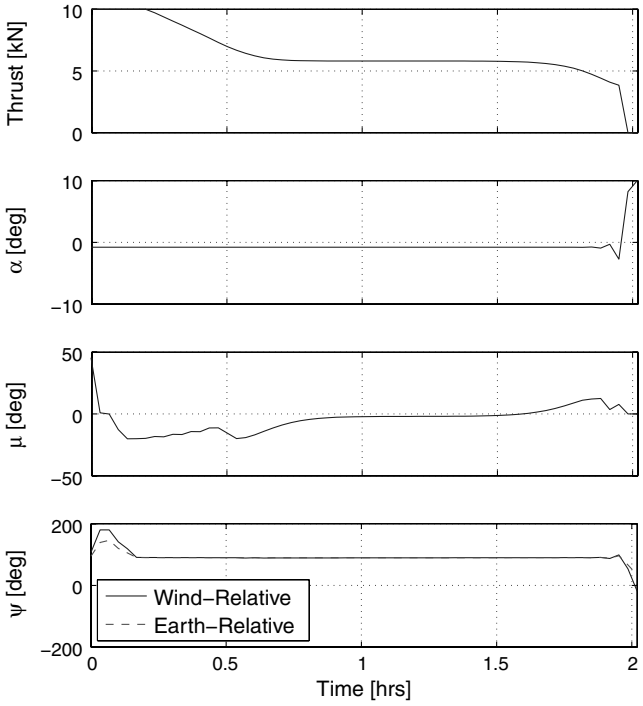

Fig. 6 Scenario 2, control history for minimum-time solution.

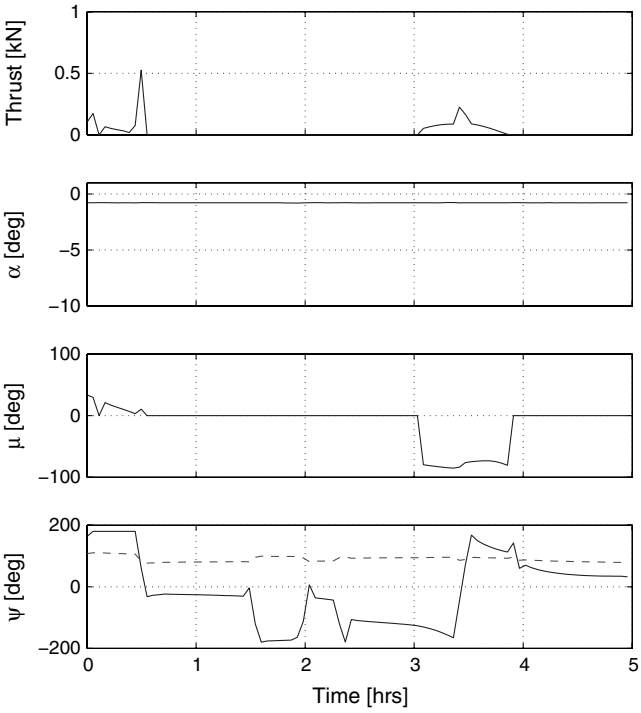

Fig. 8 Scenario 2, control history for minimum-energy solution.

A. Characteristics of Optimal Flights

We first consider ascent trajectories for two different launch sites, with scenario 1 launching from 20 km east of the target and scenario 2 launching from 250 km west of the target. For each scenario, we consider both minimum-time and minimum-energy flights. Minimum-time ascent flights may be necessary for military missions, in which the airship is at risk at low altitudes, or for any time-sensitive application in which the payload must be delivered to operational altitude as soon as possible. Minimum-energy flights, on the other

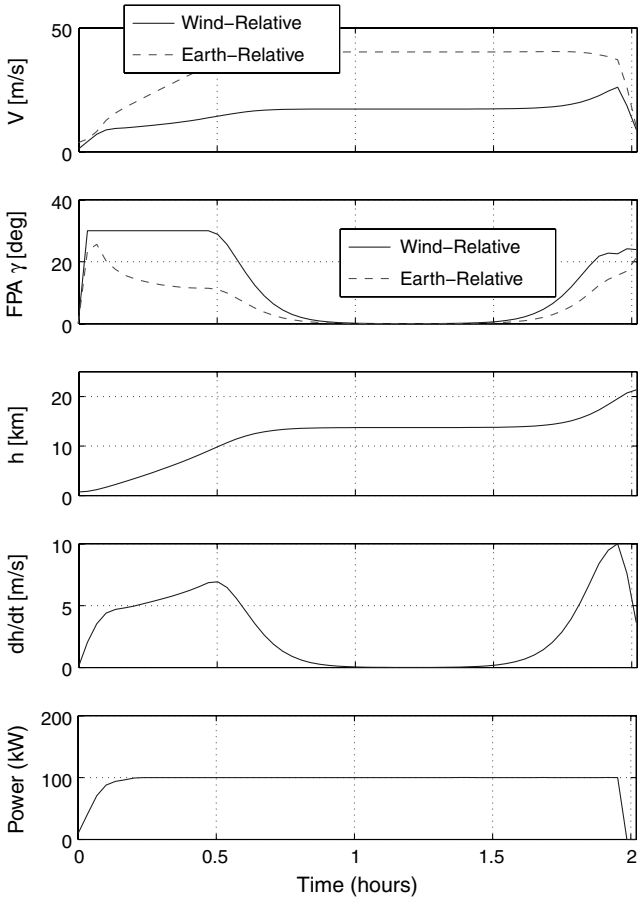

Fig. 7 Scenario 2, selected time histories for minimum-time solution.

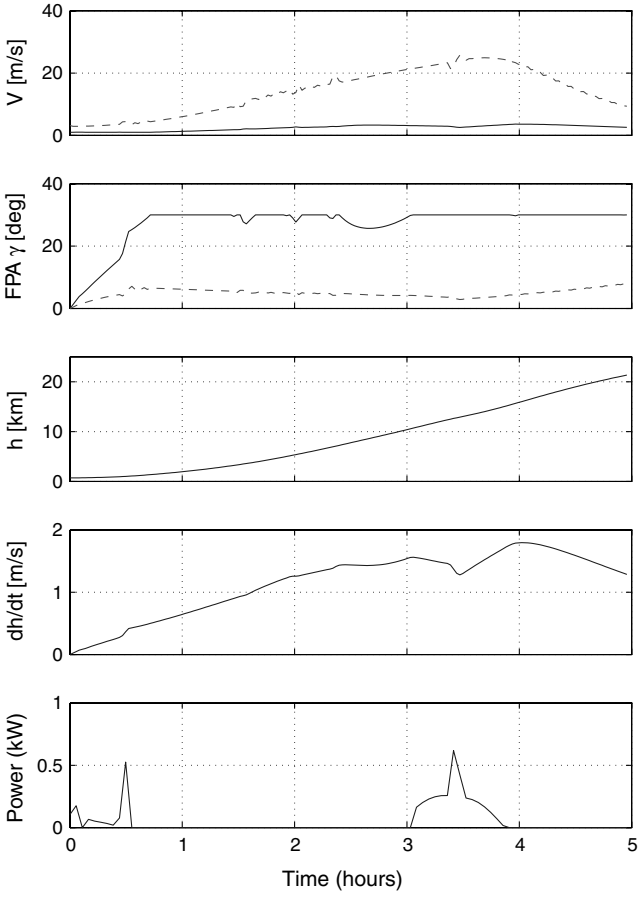

Fig. 9 Scenario 2, selected time histories for minimum-energy solution.

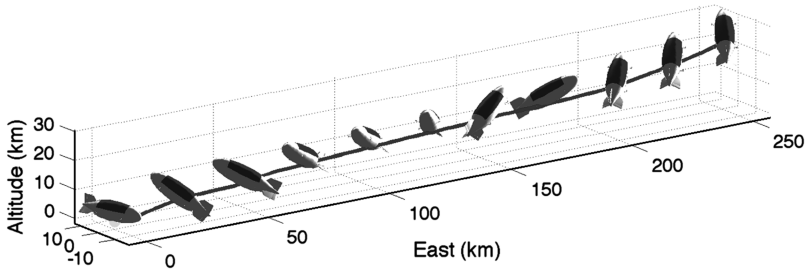

Fig. 10 Scenario 2, minimum-energy 3-D ascent trajectory.

hand, would be important for situations when the airship has limited power-production capability, such as night launches.

Scenarios 1 and 2 are illustrated in Fig. 5, in which the vertical axis is shown with a larger scale for clarity. Recall that the wind pattern is directed east across all altitudes, with a maximum velocity occurring at around 14 km, as shown in Fig. 4. In scenario 1, the airship must fly against the wind to reach the target. The minimum-time solution takes 1 h and 10 min, with the airship flying at the maximum flight-path angle of 30 deg and using maximum power for the duration of the flight. Although the wind blows the airship further east of its launch point, the airship wind-relative heading is aligned west at all times.

In scenario 2, the airship launches much further away at 250 km, but is able to fly with the wind for the entire flight. The minimum-time trajectory takes 2 h. The airship first saturates thrust at 10 kN, then immediately reaches the maximum flight-path angle of 30 deg. It continues to accelerate and reaches the power limit of 100 kW after 12 min. It then cruises at the jet-stream altitude of 14 km for about 45 min, covering a range of 120 km, and finally climbs to the target station. The control history for this minimum-time case of scenario 2 is shown in Fig. 6, and time histories for velocity, flight-path angle, climb rate, and power are shown in Fig. 7. The Earth-relative heading, flight-path angle, and velocity are shown as dashed lines.

It is interesting to observe the use of angle of attack as a control. In this and in all other simulations, the angle of attack is set to -0.78 deg for almost the entire trajectory, which is the minimum drag angle for the polynomial approximation of drag coefficient used from [5]. Longitudinal control is achieved primarily by throttling thrust and rotating the thrust vector through μ. Aerodynamic lift and drag are used sparingly. In this case, angle-of-attack control is used only at the end of the trajectory to reduce speed, so that the final Earth-relative velocity constraint of less than 10 m/s can be met.

For the minimum-energy flight of scenario 2, the control histories are plotted in Fig. 8, and additional time histories are given in Fig. 9. The trajectory begins with the airship flying 1 m/s to the east. Although the airspeed stays below 5 m/s during the flight, the Earth-relative velocity increases to nearly 30 m/s before decreasing to the maximum terminal constraint of 10 m/s. A sequence of small thrusts is applied in the first half-hour to initiate the climb. The airship continues to climb at the maximum flight-path angle for the duration of the flight. A small amount of downward thrust is applied again between 3 and 4 h to prevent the flight-path angle from increasing above its limit. The airspeed velocity is seen to increase steadily throughout the flight, even when no thrust is applied. This is possible because the minimum-energy solution intentionally avoids the use of thrust and instead exploits the accelerations due to mass-flow rate, Coriolis effects, and wind rates. The Earth-relative heading stays near 90 deg for the entire flight, as the airship always travels east with the wind, although the wind-relative heading changes several times.

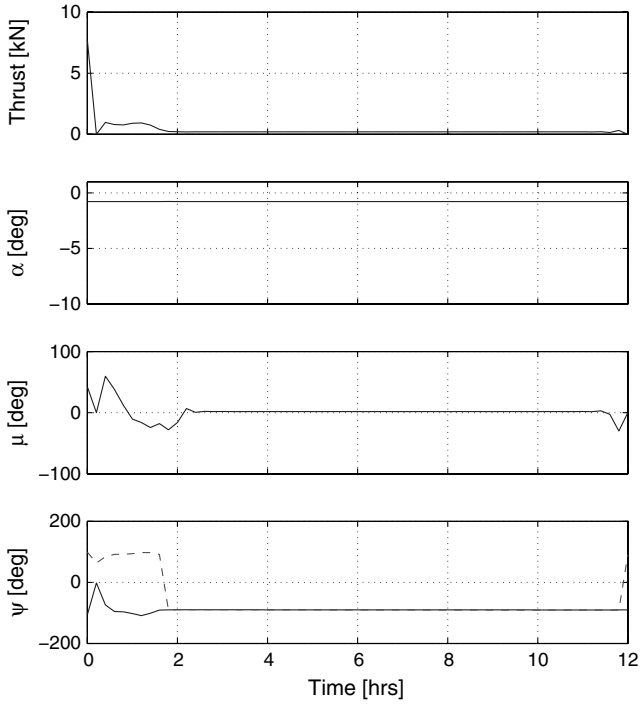

Fig. 11 Scenario 1, control history for minimum-energy solution.

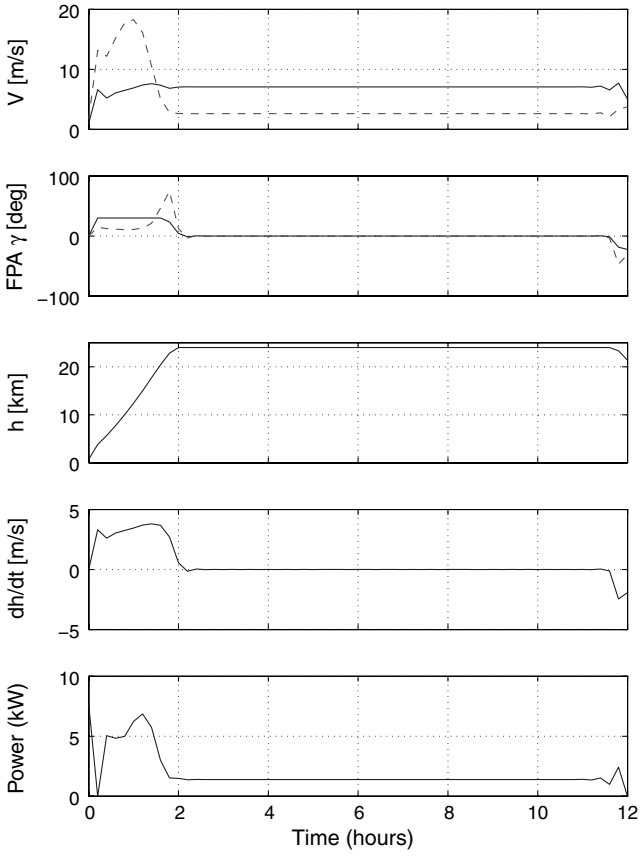

Fig. 12 Scenario 1, selected time histories for minimum-energy solution.

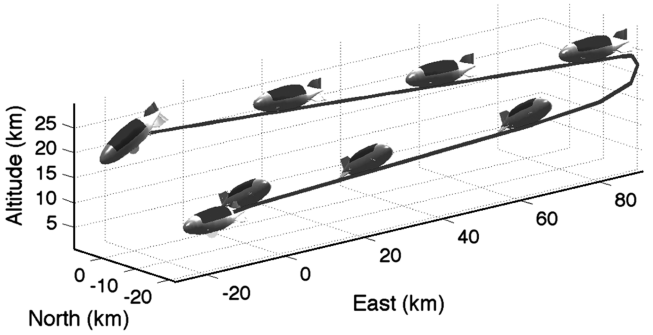

Fig. 13 Scenario 1, minimum-energy 3-D ascent trajectory.

When the airship flies north or south, the wind rate terms vanish because the wind model used here is only directed to the east. In addition, the heading angle has a direct impact on the magnitude of Coriolis acceleration in the x direction. In this way, the heading angle provides a small amount of longitudinal control. A perspective view of the ascent trajectory for this scenario is shown in Fig. 10. It illustrates the changing wind-relative heading of the airship during its ascent.

For scenario 1, in which the launch location is 20 km downwind, the airship is carried past the target by the wind. It therefore must expend a certain amount of energy to return to the target, regardless of the time of flight. The control history for the minimum-energy solution of scenario 1 is given in Fig. 11, and additional time histories are provided in Fig. 12. The first 2 h are spent climbing to the pressure altitude of 24 km. The Earth-relative heading angle during this time is at 90 deg, meaning that the airship flies east with the wind as it climbs. Once it reaches the maximum altitude, just before 2 h, it turns west and flies at about 7 m/s for the next 10 h, covering a distance of over 90 km, until it finally descends to the target station. A perspective view of the ascent trajectory is shown in Fig. 13, which shows the changing wind-relative heading of the airship as it climbs and turns.

It is interesting to compare the relative magnitude of the various components of acceleration that the airship experiences. Consider the acceleration in the x direction of the wind frame for the minimum-time and minimum-energy (5 h) solutions of scenario 2, as shown in Fig. 14. The effects due to mass-flow rate and wind rates are clearly comparable with the net effect of thrust and drag. For the minimum-time solution, the maximum acceleration due to Earth's rotation is about 1 order of magnitude smaller than the other components, at 1 E-03. For the minimum-energy solution, however, its magnitude is comparable with the other components. Although the effects of Earth rotation and mass-flow rate do not provide a dominating influence, these relative magnitudes suggest that they ought to be incorporated into the trajectory planning process along with the wind rates.

B. Time and Energy Tradeoff

For scenarios 1 and 2, we now consider minimum-energy trajectories at a series of specified flight times, extending to a maximum flight time of 12 h. Figure 15 shows the initially steep and then gradual energy reduction with increasing flight time for both scenarios. For scenario 1, the energy continues to decrease with increasing the flight time, but extending the flight to 16 h provides only a 2.5% further decrease in energy. The minimum-energy solutions of scenario 1 follow a similar path to that of the minimum-time case, but climb at slower airspeeds to reduce drag, which results in the jet-stream winds carrying the airship further east. In all cases, the optimal trajectory involves a direct climb to the maximum operational altitude of 24 km, followed by a cruise and descent to the target station.

For the minimum-energy trajectories of scenario 2, there is a steep decline in the energy requirement from 2 to 4 h. The energy reaches a minimum between 5 and 6 h and then gradually increases with larger flight time. The zoomed-in view of the energy curve for scenario 2 clearly shows the energy increasing after 6 h. The minimum-energy solution requires just 0.5% of the energy required for the minimum-time case. For this solution, the vehicle climbs slowly at low airspeeds, eventually entering the jet stream and allowing the wind to carry it to the target. For flight times less than 5–6 h, additional energy must be expended to increase the eastward velocity. For longer flight times, additional energy is required to decrease the eastward velocity. In general, the airspeeds stay very low, between 1–4 m/s, so that there is very little drag (100–350 N). The small deceleration due to this drag is comparable with the accelerations associated with wind rate, Coriolis effect, and mass-flow rate. Thus, thrust is used sparingly to maintain a small positive rate of climb as it coasts to the target.

These results indicate that, unless seriously pressed for time, optimal airship ascent operations should be designed at the minimum-energy points, with a maximum flight time constraint applied if necessary. At these conditions, the energy consumption is greatly reduced for a reasonable time penalty.

C. Effects of Varying Initial Positions

The previous sections focus on scenarios that primarily involve east/west motion with an eastward wind. We now consider the effect of changing the initial heading of the launch location. In scenario 3, trajectories are planned for launch sites distributed along a circular region with the radius of 10 km from the target, and in scenario 4 the radius is increased to 100 km.

A set of 12 different trajectories is shown in Fig. 16 for the 10-km-range case. The shaded bar on the side of the figure is provided to illustrate the flight time of each trajectory. The left plot shows the horizontal projection of each path, and the right plot provides a perspective view. As we would expect, initial positions to the west of

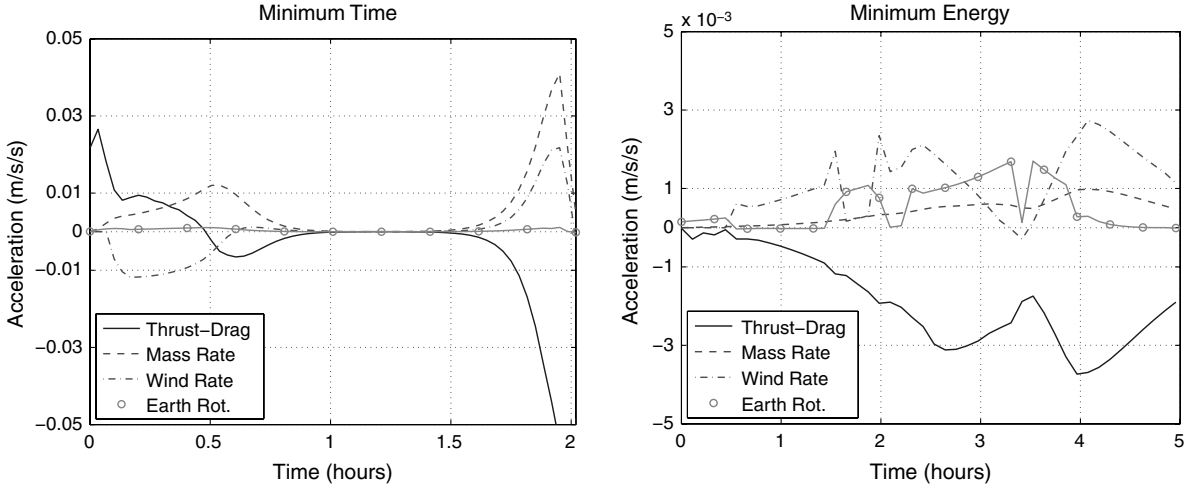

Fig. 14 Scenario 2, acceleration components for minimum-time and minimum-energy solutions.

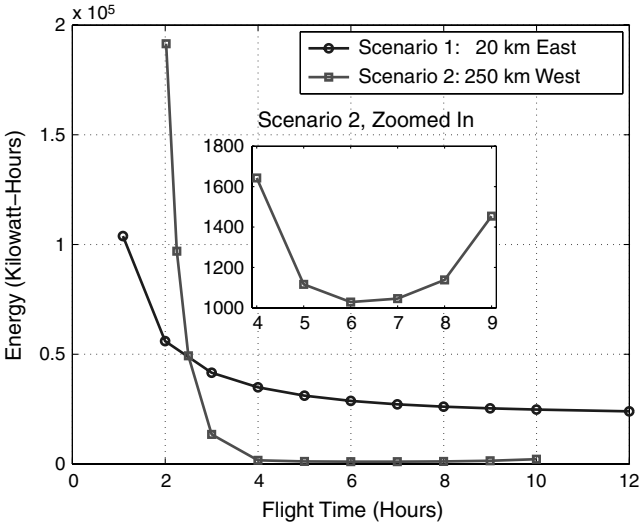

Fig. 15 Scenarios 1 and 2, energy vs time.

the target location result in shorter flight times, as they enable airships to fly with the wind during most of the flight. The trajectory launched from the due west location winds back and forth during its ascent. This is necessary to achieve the maximum climb rate while preventing the airship from flying too far east, much like winding up or down a mountain with a fixed slope.

Similar results are observed for the 100-km-range case, scenario 4. A set of 24 trajectories is shown in Fig. 17, with the flight time ranging from about 1 to 2 h. Here, we also observe a transition between two types of trajectories. For the launch sites located furthest to the west, the minimum-time ascent involves a consistent climb to the target altitude, with a greater distance covered in the jet-stream altitudes. However, as the launch point moves east, the nature of the optimal solution changes. As the launch position moves around the circle toward the east, we reach a condition in which the fastest path involves first climbing above the target altitude to the altitude ceiling, then descending to the station. Note that this is the type of altitude profile observed for all cases of scenario 1. The reason for this behavior is due to the fact that the maximum power constraint for the minimum-time solution is active for nearly the entire flight (see Fig. 6). With the power constraint reached, the only way to increase the velocity is to reduce the thrust. This is only possible by elevating to lower-density air when the drag for a given velocity is lower.

In Fig. 18, we see that the flight time and total energy follow the same trend with launch location. This is to be expected, because in all cases, the objective is to minimize flight time. The associated structure of the control is also the same in all cases, with the power constraint active for nearly the entire flight. Thus, the total energy (the integral of the power) is expected to depend linearly on the flight time.

Clearly, the jet stream provides a speed advantage only if the final altitude could be reached before the final longitude is reached. In these cases, the airship can reduce the rate of climb while in the jet-stream altitudes to use the wind. This is seen in the far west launch locations of scenario 4 and in the minimum-time solution of scenario 2. Here, the launch location is far enough away that, with the fastest possible climb, the final altitude would be reached before the final longitude is reached. Otherwise, there is no advantage to staying in the jet stream, and the optimal solution is simply to climb as fast as possible. Because the jet-stream winds carry the airship further east of the target station in these cases, the final phase of the flight involves flying into the wind at maximum power and sometimes at maximum airspeed. This final return phase involves a cruise at the maximum altitude at which the resisting wind and density is smallest.

D. Discussions

Results obtained in this paper are specific to the wind model and airship configuration that was used. However, the wind model is representative of the class of wind profiles that are seen throughout many parts of the globe, and the airship design is based upon published data from prototype vehicles as well as accumulated engineering experience from prior work in airship research. Therefore, examination of these optimization results enables us to develop some general strategies for planning optimal ascent trajectories subject to similar wind profiles and similar vehicle designs.

There are also some important limitations to the scope of this analysis. First, neutral buoyancy has been assumed at all flight conditions, which requires the pressure regulation system to achieve high mass-flow rates during high rates of climb or, more precisely, whenever the rate of change in the ambient-air density is high. A more accurate model would include airflow constraints, so that buoyancy and weight are modeled separately. In such a model, neutral-buoyancy conditions would only be achieved when the required mass-flow rate is under the prescribed limit. Also, as previously mentioned, our model for the required power for flight does not include the operation of fans for pressure regulation. Including this power requirement in the performance objective would lead to more accurate predictions of energy consumption and may influence the optimal trajectories. Finally, the power generation during the flight of a stratospheric airship depends upon its orientation, which governs the incidence angles of the photovoltaic solar cells. Introducing a model for the generated power and including appropriate energy-balance constraints may lead to a different class of optimal trajectories that exploit the combination of the wind-relative and inertial orientations as the sun moves through the sky. Each of these areas are topics worthy of future research.

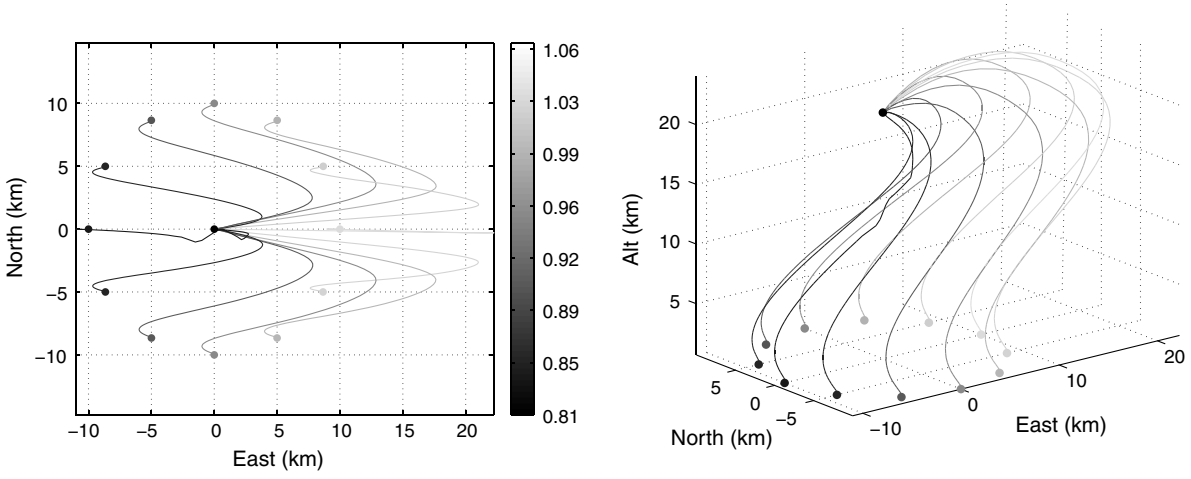

Fig. 16 Scenario 3, minimum-time ascent trajectories from 10 km radius.

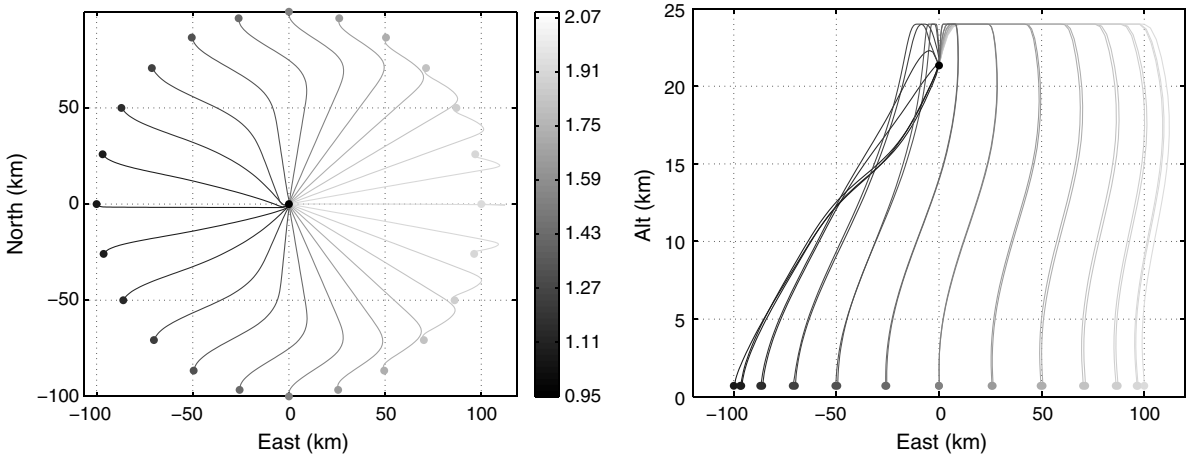

Fig. 17 Scenario 4, minimum-time ascent trajectories from 100 km radius.

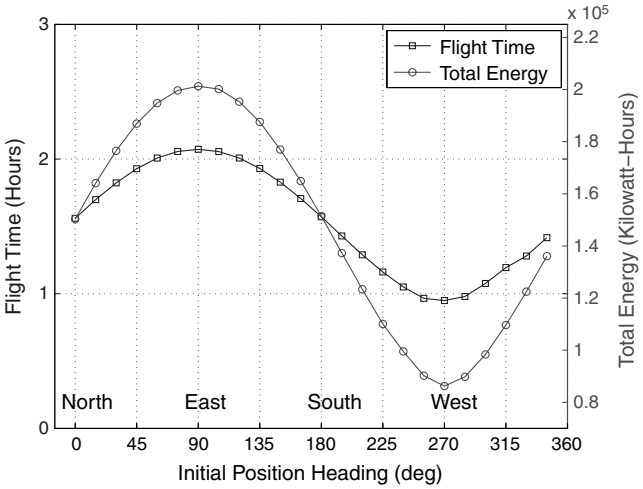

Fig. 18 Scenarios 4, energy and time vs launch location.

VIII. Conclusions

This paper develops the equations of motion for an airship in the presence of horizontal winds and presents the solutions for optimal ascent trajectories under various conditions. Airship ascent flights in wind are formulated as nonlinear optimal control problems that minimize flight time and energy consumption. These problems are converted into nonlinear parameter optimization problems and are solved using SNOPT.

Extensive numerical solutions illustrated several interesting trends. It is clear that the high-velocity winds in the jet-stream altitude range (10–14 km) have a major impact on all optimal trajectories. Minimum-time solutions typically reach constraint limits in a consistent sequence: thrust, flight-path angle, power, climb rate, and airspeed. Minimum-energy solutions with a fixed final time slightly above the minimum-time solution can provide a substantial energy savings. In general, the minimum-energy solution is to fly at very low airspeeds with a steady rate of climb, using wind rates and mass-flow rate whenever possible. There is also a general trend for minimum-time trajectories that can use jet-stream winds versus those that cannot use them. Solutions that cannot benefit from the jet-stream winds first climb to the maximum altitude and then return to the station flying against the wind at maximum altitude. If the wind can be used, on the other hand, the minimum-time solution always reduces the rate of climb while in the jet stream. These observations should hold true for similar airship configurations and similar wind profiles.

It is clear that the optimal airship ascent trajectories are strong functions of both the wind environment and the imposed constraints on thrust, power, and rate of climb. Therefore, future work on this topic should include an analysis of performance sensitivity to modeling parameters, performance limits, and uncertainty in the wind velocities. Given the need to design optimal trajectories subject to uncertain wind conditions, a robust trajectory planning approach is desired. In addition, incorporating the power requirement and airflow constraints for the pressure regulation system would provide a more realistic model for weight and power consumption and more accurate minimum-energy solutions.

Acknowledgments

This work was supported in part by a research grant from the National Science Foundation, award no. CCF—0515009, and by a NASA cooperative agreement, NNG05GG39H.

References

[1] Colozza, A., "Initial Feasibility Assessment of a High Altitude Long Endurance Airship," NASA CR-2003-212724, Dec. 2003.

[2] Schmidt, D. K., Stevens, J., and Roney, J., "Near-Space Station-Keeping Performance of a Large High-Altitude Notional Airship," *Journal of Aircraft*, Vol. 44, No. 2, Apr. 2007, pp. 611–615. doi:10.2514/1.24863

[3] Tozer, T. C., and Grace, D., "High Altitude Platforms for Wireless Communications," *Electronics and Communication Engineering Journal*, Vol. 13, No. 3, June 2001, pp. 127–137. doi:10.1049/ecej:20010303

[4] Miller, C., Sullivan, J., and McDonald, S., "High Altitude Airship Simulation Control and Low Altitude Flight Demonstration," AIAA Infotech@Aerospace, Rohnert Park, CA, AIAA Paper 2007-2766, May 2007.

[5] Lee, S., and Bang, H., "Three-Dimensional Ascent Trajectory Optimization for Stratospheric Airship Platforms in the Jet Stream," *Journal of Guidance, Control, and Dynamics*, Vol. 30, No. 5, 2007, pp. 1341–1352. doi:10.2514/1.27344

[6] Lutz, T., and Wagner, S., "Drag Reduction and Shape Optimization of Airship Bodies," *Journal of Aircraft*, Vol. 35, No. 3, 1998, pp. 345–351. doi:10.2514/2.2313

[7] Gomes, S., and Ramos, J., "Airship Dynamic Modeling for Autonomous Operation," *IEEE International Conference on Robotics and Automation*, Vol. 4, Inst. of Electrical and Electronics Engineers, Piscataway, NJ, May 1998, pp. 3462–3467. doi:10.1109/ROBOT.1998.680973

[8] Battipede, M., and Gil, P., "Peculiar Performance of a New Lighter-Than-Air Platform for Monitoring," 3rd Unmanned Unlimited Technical Conference, Workshop and Exhibit, Chicago, AIAA Paper 6448, Sept. 2004.

[9] Schmidt, D. K., "Modeling and Near-Space Stationkeeping Control of a Large High-Altitude Airship," *Journal of Guidance, Control, and Dynamics*, Vol. 30, No. 2, 2007, pp. 540–547. doi:10.2514/1.24865

[10] Lee, S., Lee, H., Won, D., and Bang, H., "Backstepping Approach of

Trajectory Tracking Control for the Mid-Altitude Unmanned Airship," AIAA Guidance, Navigation and Control Conference and Exhibit, Hilton Head, SC, AIAA Paper 2007-6319, Aug. 2007.

[11] Repoulias, F., and Papadopoulos, E., "Dynamically Feasible Trajectory and Open-Loop Control Design for Unmanned Airships," *Mediterranean Conference on Control and Automation*, Inst. of Electrical and Electronics Engineers, Piscataway, NJ, June 2007, pp. 1–6. doi:10.1109/MED.2007.4433820

[12] Rooz, N., and Johnson, E., "Design and Modelling of An Airship Station Holding Controller for Low Cost Satellite Operations," AIAA Guidance, Navigation, and Control Conference and Exhibit, San Francisco, AIAA Paper 2005-6200, Aug. 2005.

[13] Kim, J., Keller, J., and Kumar, V., "Design and Verification of Controllers for Airships," *IEEE/RSJ International Conference on Intelligent Robots and Systems*, Vol. 1, Inst. of Electrical and Electronics Engineers, Piscataway, NJ, Oct. 2003, pp. 54–60. doi:10.1109/IROS.2003.1250605

[14] Hygounenc, E., and Soueres, P., "Automatic Airship Control Involving Backstepping Techniques," *IEEE International Conference on Systems, Man and Cybernetics*, Vol. 6, Inst. of Electrical and Electronics Engineers, Piscataway, NJ, Oct. 2002.

[15] Sharma, S., Kulczycki, E., and Elfes, A., "Trajectory Generation and Path Planning for Autonomous Aerobots," Jet Propulsion Lab., California Inst. of Technology, Pasadena, CA, 2007.

[16] Hima, S., and Bestaoui, Y., "Motion Generation on Trim Trajectories for an Autonomous Underactuated Airship," *4th International Airship Convention and Exhibition* [CD-ROM], Airship Association, July 2002.

[17] Kampke, T., and Elfes, A., "Optimal Aerobot Trajectory Planning for Wind-Based Opportunistic Flight Control," *IEEE/RSJ International Conference on Intelligent Robots and Systems*, Vol. 1, Inst. of Electrical and Electronics Engineers, Piscataway, NJ, Oct. 2003, pp. 67–74.

[18] Zhao, Y. J., Garrard, W. L., and Mueller, J. B., "Benefits of Trajectory Optimization in Airship Flights," 3rd AIAA "Unmanned Unlimited" Technical Conference, Workshop and Exhibit, AIAA, Reston, VA, 2004, pp. 1–14.

[19] Mueller, J. B., and Zhao, Y. J., "Development of an Aerodynamic Model and Control Law Design for a High-Altitude Airship," 3rd AIAA "Unmanned Unlimited" Technical Conference, Workshop and Exhibit, AIAA, Chicago, AIAA Paper 6479, 2004.

[20] Khoury, G. A., and Gillett, J. D., *Airship Technology*, Cambridge Aerospace Series, 10, Cambridge Univ. Press, New York, 1999.

[21] Tuckerman, L. B., "Inertia Factors of Ellipsoids for Use in Airship Design," NACA Rept. 210, 1926.

[22] "U.S. Standard Atmosphere 1976," National Oceanic and Atmospheric Administration, TR NOAA-S T 76-15672, Washington, D.C., 1976.

[23] Hedin, A. E., Fleming, E. L., Manson, A. H., Schmidlin, F. J., Avery, S. K., Clark, R. R., Franke, S. J., Fraser, G. J., Tsuda, T., Vial, F., and Vincent, R. A., "Empirical Wind Model for the Upper, Middle and Lower Atmosphere," *Journal of Atmospheric and Terrestrial Physics*, Vol. 58, No. 13, Sept. 1996, pp. 1421–1447. doi:10.1016/0021-9169(95)00122-0

[24] Betts, J., "Survey of Numerical Methods for Trajectory Optimization," *Journal of Guidance, Control, and Dynamics*, Vol. 21, No. 2, 1998, pp. 193–207. doi:10.2514/2.4231

[25] Hull, D., "Conversion of Optimal Control Problems into Parameter Optimization Problems," *Journal of Guidance, Control, and Dynamics*, Vol. 20, No. 1, 1997, pp. 57–60. doi:10.2514/2.4033

[26] Herman, A., and Conway, B., "Direct Optimization Using Collocation Based on High-Order Gauss-Lobatto Quadrature Rules," *Journal of Guidance, Control, and Dynamics*, Vol. 19, No. 3, 1996, pp. 592–599. doi:10.2514/3.21662

[27] Murray, W., Gill, P. E., and Saunders, M. A., "SNOPT: An SQP Algorithm for Large-Scale Constrained Optimization," *SIAM Journal on Optimization*, Vol. 12, No. 4, 2002, pp. 979–1006. doi:10.1137/S1052623499350013